

# Cluster rearrangement by chiral charge order in lacunar spinel $\text{GaNb}_4\text{Se}_8$

Shunsuke Kitou,<sup>1,\*</sup> Masaki Gen,<sup>2</sup> Yuiga Nakamura,<sup>3</sup> Yusuke Tokunaga,<sup>1</sup> Taka-hisa Arima<sup>1,2</sup>

<sup>1</sup>*Department of Advanced Materials Science, The University of Tokyo, Kashiwa 277-8561, Japan.*

<sup>2</sup>*RIKEN Center for Emergent Matter Science, Wako 351-0198, Japan.*

<sup>3</sup>*Japan Synchrotron Radiation Research Institute (JASRI), SPring-8; Hyogo 679-5198, Japan.*

## ABSTRACT

Transition-metal atoms with  $d$  electrons sometimes form clusters in crystals, which significantly affects the physical properties. Such a cluster formation frequently accompanies a change in the crystal system, leading to the presence of domains with different crystal orientations. In particular, the cubic symmetry is rarely retained after the cluster formation. Here, we identify a cubic-to-cubic phase transition in lacunar spinel  $\text{GaNb}_4\text{Se}_8$ , where the change in the lattice parameter is less than 0.0001%. Each  $\text{Nb}^{3.25+}$  tetramer with seven  $4d$  electrons is distorted into a  $\text{Nb}^{3+}$  trimer and a  $\text{Nb}^{4+}$  monomer induced by charge disproportionation among Nb ions. While the  $\text{Nb}^{3+}$  trimer with six  $4d$  electrons forms spin-singlets in the  $\sigma$ -bonding orbitals for three Nb—Nb bonds, a localized  $S = 1/2$  spin remains on the  $\text{Nb}^{4+}$  ion. Furthermore, a local electric dipole moment is induced along the three-fold rotation axis of each distorted tetramer by the cluster rearrangement. The electric dipole moments are regularly arranged to maintain the cubic symmetry, giving rise to chiral order.

## INTRODUCTION

Transport and magnetic properties in transition-metal chalcogenides are dominated by the orbital state of transition metals surrounded by chalcogen elements O, S, and Se. Early transition-metal atoms sometimes form clusters,<sup>1,2</sup> lowering the energy by sharing bonding  $d$  electrons. For instance, rutile-type vanadium dioxide  $\text{VO}_2$  with a tetragonal lattice undergoes a metal-insulator transition due to V-V dimerization,<sup>3-7</sup> resulting in monoclinic distortion of

the entire lattice. In general, structural phase transitions involving the cluster formation cause large local distortion, leading to significant anisotropic deformation of the overall lattice.

$\beta$ -pyrochlore oxide  $\text{CsW}_2\text{O}_6$  is a rare material that preserves the cubic lattice symmetry across the phase transition accompanied by cluster formations.  $\text{CsW}_2\text{O}_6$  with a half-integer average valence of  $\text{W}^{5.5+}$  ( $5d^{0.5}$ ) undergoes a metal-insulator transition at 215 K,<sup>8,9</sup> where the space group changes from  $Fd\bar{3}m$  to  $P2_13$ . The pyrochlore network of  $\text{W}^{5.5+}$  in the higher-temperature cubic phase is distorted three-dimensionally to form regular  $\text{W}^{5.33+}$  ( $5d^{2/3}$ ) trimers and isolated  $\text{W}^{6+}$  ( $5d^0$ ) ions in the lower-temperature cubic phase, where the lattice constant increases by  $\sim 0.004\%$  with the cubic-to-cubic phase transition. The  $\text{W}^{5.33+}$  trimer has two  $5d$  electrons, indicating a three-centered-two-electron bond formation.<sup>9</sup> Such a cluster formation leads to the non-magnetic insulating nature in the lower-temperature cubic phase. In this system, the cubic symmetry is maintained by orienting adjacent  $\text{W}$  trimers not parallel to each other.

Lacunar spinel compounds  $\text{GaM}_4\text{X}_8$  ( $M = \text{V}, \text{Nb}, \text{Mo}, \text{Ta}$ , and  $X = \text{S}, \text{Se}$ ) are Mott insulator systems that exhibit various electronic and magnetic properties, such as pressure-induced superconductivity,<sup>10-13</sup> spin-singlet state,<sup>14,15</sup> spin-orbit entangled molecular  $J_{\text{eff}}$  state,<sup>15-20</sup> and magnetic skyrmions.<sup>21-24</sup> Since the formal valence of  $M$  is 3.25+, the average number of  $d$  electrons are 7/4 and 11/4 for group V ( $M = \text{V}, \text{Nb}, \text{Ta}$ ) and group VI ( $M = \text{Mo}$ ) transition metals, respectively. Since only half of the tetrahedral sites are occupied by Ga atoms, the pyrochlore network of  $M$  atoms takes on a breathing-type structure, resulting in  $M_4$  tetrahedral clusters. The space group is noncentrosymmetric  $F\bar{4}3m$ . As cooling  $\text{GaM}_4\text{X}_8$  with  $M = \text{V}$  and  $\text{Mo}$ , the overall lattice is distorted along one of the cubic  $\langle 111 \rangle$  axes, resulting in the rhombohedral polar  $R3m$  space group.<sup>25</sup> This rhombohedral distortion is understood as a cooperative Jahn-Teller distortion of the  $M_4$  molecular orbitals. Furthermore, in a magnetic field, magnetic orders including a skyrmion lattice emerge at lower temperatures in the rhombohedral phase.<sup>21-24</sup> In contrast,  $\text{GaM}_4\text{X}_8$  with  $M = \text{Nb}$  and  $\text{Ta}$  exhibit different types of distortion. The lattice of  $\text{GaTa}_4\text{Se}_8$  changes to tetragonal below  $T_M = 50$  K.<sup>15,20</sup>  $\text{GaNb}_4\text{S}_8$  and  $\text{GaNb}_4\text{Se}_8$  have orthorhombic distortion in the low-temperature phase below  $T_M = 32$  and 33 K, respectively.<sup>15,26</sup> These low-temperature phases are characterized by non-magnetic (spin-singlet)

nature confirmed by nuclear magnetic resonance.<sup>14,15</sup> However,  $\text{GaNb}_4\text{Se}_8$  undergoes another phase transition at  $T_C = 50$  K.<sup>15</sup> Powder X-ray diffraction (XRD) experiments suggest the cubic space group  $P2_13$  in the intermediate-temperature phase between  $T_M$  and  $T_C$ .<sup>15</sup>

In this study, we perform single-crystal synchrotron XRD experiments to reveal the crystal structure in the intermediate-temperature phase of  $\text{GaNb}_4\text{Se}_8$ . Nb clusters are found to be rearranged to form chiral charge order associated with charge disproportionation among Nb ions. The cubic-to-cubic phase transition maintains the overall lattice and total magnetic moment with an exquisite cluster rearrangement, which is different from the first-order phase transition to a non-magnetic state in  $\text{CsW}_2\text{O}_6$ .<sup>9</sup>

## Experiments

Polycrystalline samples of  $\text{GaNb}_4\text{Se}_8$  were synthesized by a solid-state reaction of high-purity ingredients Ga (99.99%), Nb (99.9%), and Se (99.999%). The stoichiometric powder was sealed in an evacuated quartz ampoule and heated at 900 °C for 70 h. The polycrystalline material was used as a source for a single-crystal growth by chemical vapor transport. The growth was performed using  $\text{PtCl}_2$  as a transport agent in a quartz ampoule at temperatures between 900 and 950 °C for 240 h. Magnetization measurements were performed by a superconducting quantum interference device (MPMS, Quantum Design) between 2 and 300 K in magnetic fields up to 7 T. Heat capacity was measured by the thermal relaxation method by using a commercial system (Quantum Design: PPMS). Thermal expansion along the [111] axis was measured by the fiber-Bragg-grating (FBG) technique using an optical sensing instrument (Hyperion si155, LUNA) in a cryostat equipped with a superconducting magnet (Oxford Spectromag). XRD experiments were performed using a single crystal of  $52 \times 48 \times 35 \mu\text{m}^3$  on BL02B1 at a synchrotron facility SPring-8 in Japan.<sup>27</sup> A He-gas-blowing device was employed for controlling the temperature between 34 and 300 K. The X-ray wavelength was  $\lambda = 0.30956 \text{ \AA}$ . A two-dimensional detector CdTe PILATUS was used to record the diffraction pattern. The intensities of Bragg reflections with the interplane distance  $d > 0.28 \text{ \AA}$  were collected by CrysAlisPro program.<sup>28</sup> Intensities of equivalent reflections

were averaged and the structural parameters were refined by using Jana2006.<sup>29</sup> Crystal structures are visualized by using VESTA.<sup>30</sup>

## Results and Discussions

Figures 1a and 1b show the crystal structure of GaNb<sub>4</sub>Se<sub>8</sub> at 70 K in the high-temperature phase. Merohedral domains corresponding to space inversion were not observed. The deficiency of the Ga site is found to be less than 1%. Nb atoms form regular tetrahedra. The intra- and inter-clusters distances between Nb atoms are 3.0345(4) and 4.3295(5) Å, respectively. Details of the structural parameters are summarized in Tables S1 and S2 in Supporting Information. Figure 1c shows the molecular orbital scheme of a Nb<sub>4</sub> cluster. The *t*<sub>2g</sub> atomic orbitals of a Nb ion in a regular Se<sub>6</sub> octahedron split into five types of molecular orbitals with different energies under *T<sub>d</sub>* symmetry due to the Nb<sub>4</sub> cluster formation.<sup>31</sup> The *t*<sub>2</sub> molecular orbitals accommodate one electron, resulting in an *S* = 1/2 state when ignoring spin-orbit interaction.

Figure 2a shows the temperature dependence of magnetic susceptibility  $\chi$  for  $H \parallel [111]$  of GaNb<sub>4</sub>Se<sub>8</sub>. There is no anisotropy in the magnetic susceptibility when the external magnetic fields are applied in the [111], [110], and [001] directions (Figure S1 and Table S5 in Supporting Information). We perform a Curie-Weiss fit for the magnetic susceptibility curve using a formula  $\chi(T) = \chi_0 + C/(T - \Theta)$ , where  $\chi_0$ , *C*, and  $\Theta$  are temperature independent component of  $\chi$ , Curie constant, and Weiss temperature, respectively. The fit above 150 K yields  $\chi_0 = -6.2 \times 10^{-5}$  emu/mol, *C* = 0.3033 K emu/mol, and  $\Theta = -142.6$  K. The Curie constant gives the effective magnetic moment  $\mu_{\text{eff}} = 1.558\mu_{\text{B}}/\text{f. u.}$ , which is slightly smaller than the expected value  $1.73\mu_{\text{B}}/\text{f. u.}$  for *S* = 1/2. A kink and a sharp decrease are observed in  $\chi$  at  $T_{\text{C}} = 50$  K and  $T_{\text{M}} = 31$  K, respectively. These results are consistent with previous reports.<sup>15,32</sup> A thermal hysteresis indicates first-order nature of the phase transition around  $T_{\text{M}}$ , as shown in the inset of Figure 2a. Furthermore,  $T_{\text{M}}$  slightly decreases with increasing the external magnetic field (Figure S2 in Supporting Information).

Figure 2b shows the temperature dependence of heat capacity divided by temperature ( $C_p/T$ ) at 0 T. Broad and sharp peaks are observed at  $T_{\text{C}}$  and  $T_{\text{M}}$ , which indicate second- and

first-order phase transitions, respectively. The low-temperature behavior deviates from the Debye model ( $C_p \propto T^3$ ) (Figure S3a in Supporting Information). The  $C_p \propto T^2$  component appears at low temperatures, which is not a typical behavior of three-dimensional antiferromagnet, where the magnon contribution  $C_p^{\text{mag}}$  is proportional to  $T^3$ . The entropy change  $\Delta S_C = 1.0$  J/mol K associated with the second-order phase transition at  $T_C$  is estimated from  $C_p$  in  $40 \leq T \leq 50$  K. Since the heat capacity was measured by the thermal relaxation method, the released entropy in the first-order phase transition at  $T_M$  could not be accurately estimated from  $C_p$ . The entropy change at  $T_M$  is estimated from the temperature dependence and the external magnetic field dependence of the magnetic susceptibilities as  $\Delta S_M = 6.8$  J/mol K (Figure S2 in Supporting Information). In the heat capacity measurements,  $T_M$  decreases with increasing the external magnetic field (Figure S3c in Supporting Information), which is consistent with our magnetic susceptibility results and the previous report.<sup>32</sup> In contrast,  $T_C$  slightly increases with increasing the external magnetic field (Figure S3b in Supporting Information).

Figure 3a shows the temperature dependence of thermal expansion  $\Delta L/L_{300\text{K}}$  along the [111] axis of  $\text{GaNb}_4\text{Se}_8$ . While a clear increase of about 0.0002% in  $\Delta L/L_{300\text{K}}$  is observed at  $T_M$ , no anomaly is observed around  $T_C$  with a change of less than 0.0001%. Figure 3b shows the temperature dependence of the integrated intensity of a Bragg peak  $-5\ 2\ 0$ , which appears below  $T_C$ . The appearance of the Bragg reflection of  $-5\ 2\ 0$  is attributable to the change from the  $F$  to  $P$  lattice. Figures 3c and 3d show the XRD data on the  $H\ K\ 0$  plane at 70 and 40 K, respectively. Although new Bragg peaks appear at reciprocal lattice points with odd  $h$  or odd  $k$ , no peak splitting is observed for Bragg reflections in the intermediate-temperature phase. The systematic absence of Bragg peaks at  $h00$ :  $h = 2n + 1$  and at  $0k0$ :  $k = 2n + 1$  (red triangles in Figure 3d) shows  $2_1$  screw axes along the principal axes in the intermediate-temperature phase.

Figure 4a shows the crystal structure of  $\text{GaNb}_4\text{Se}_8$  at 40 K in the intermediate-temperature phase. The space group is  $P2_13$ , which is consistent with the former powder XRD experiment.<sup>15</sup> Details of the structural parameters are summarized in Tables S3 and S4 in Supporting Information. There are two distinct Nb sites, Nb1 and Nb2, with a ratio of 3:1. There

is a difference in the volumes between  $\text{Se}_6$  octahedra around Nb1 (gray) and Nb2 (orange), as shown in [Figure 4b](#), which is ascribed to the difference in the valence of Nb ions. Since the ionic radius of  $\text{Nb}^{3+}$  and  $\text{Nb}^{4+}$  are 0.72 and 0.68 Å,<sup>33</sup> Nb ions coordinated by the larger and smaller octahedra correspond to  $\text{Nb}^{3+}$  and  $\text{Nb}^{4+}$ , respectively. In the high-temperature phase, each Nb ion has 7/4 electrons in the 4*d* orbitals in average. In the intermediate-temperature phase, since  $\text{Nb}^{3+}$  and  $\text{Nb}^{4+}$  ions have two and one electrons in the 4*d* orbitals, the total number of 4*d* electrons per  $\text{Nb}_4$  cluster is  $(2e \times 3) + (1e \times 1) = 7e$ .

[Figure 4c](#) shows the molecular orbital scheme, indicating the Nb cluster rearrangement from a tetramer in the high-temperature phase to a trimer-monomer in the intermediate-temperature phase. The Nb—Nb distance in the regular tetrahedron in the high-temperature phase is 3.0345(4) Å ([Figure 1a](#)), whereas the Nb1—Nb1 and Nb1—Nb2 distances are 2.9730(4) and 3.1036(4) Å, respectively, in the distorted tetrahedron in the intermediate-temperature phase ([Figure 4d](#)). The changes in Nb—Nb distances are approximately 2%, which is significantly larger than the distortion in the overall lattice with a change of less than 0.0001%. In the distorted tetrahedron, three Nb1 atoms form a regular trimer, where two of the three  $t_{2g}$  ( $d_{yz}$ ,  $d_{zx}$ , and  $d_{xy}$ , shown by red, green, and blue ribbons, respectively, in [Figure 4e](#)) orbitals on each Nb1 site form  $\sigma$  bonds. Since a  $\text{Nb}^{3+}$  ion has two 4*d* electrons, two electrons are accommodated in each  $\sigma$ -bonding orbital,<sup>34</sup> resulting in the spin-singlet formation. These  $\sigma$ -bonding orbitals correspond to the lower-lying singlet and doublet with three up and three down electrons ([Figure 4c](#)). This type of spin-singlet trimer is reported in layered compounds  $\text{LiVO}_2$ <sup>35</sup> and  $\text{LiVS}_2$ .<sup>36</sup> A localized  $S = 1/2$  spin, represented by an orange arrow in [Figure 4c](#), remains on each Nb2 site in the intermediate-temperature phase. Therefore, each  $\text{Nb}_4$  cluster hosts  $S = 1/2$  in both the high-temperature and intermediate-temperature phases. However, the unpaired electron is tightly localized on the Nb2 site in the intermediate-temperature phase in contrast to the high-temperature phase. As a result, since the interaction between localized spins in the intermediate-temperature phase is weaker than in the high-temperature phase, the magnetic susceptibility slightly increases below  $T_C$  ([Figure 2a](#)). The phase transition at  $T_C$  does not involve changes in the cubic lattice or total magnetic moment. The entropy change  $\Delta S_C = 1.0$  J/mol K estimated from the specific heat ([Figure 2b](#)) may be

mostly attributed to a pure charge component. Considering the degeneracy of the  $t_2$  orbital with  $S = 1/2$  in the high-temperature phase (Figure 1c), the released entropy is estimated as  $R \ln 3$ . The observed  $\Delta S_C = 1.0$  J/mol K is significantly smaller than  $R \ln 3 \cong 9.1$  J/mol K, suggesting the growth of short-range interactions in the high-temperature phase.

A local electric dipole moment on the distorted Nb tetramer is shown by an orange vector in Figure 4d. The electric dipole moments are oriented in four different directions between adjacent tetramers. When viewing one (111) layer, the electric dipole moments form vortices as shown in Figure 4f, corresponding to a chiral charge order. The structural analysis revealed that two enantiomorphic domains exist in equal proportions (Table S4 in Supporting Information). These two types of domains correspond to the clockwise and counterclockwise vortices of the electric dipole moments. Figure 4f shows the domain corresponding to the counterclockwise vortices. The two domains may show the optical rotation of opposite signs.

A similar elongation of  $M_4$  tetrahedron along one three-fold rotation axis is observed in  $\text{GaV}_4\text{S}_8$ <sup>11</sup> and  $\text{GaV}_4\text{Se}_8$ ,<sup>23</sup> where a V ion has 7/4 3d electrons in average. In  $\text{GaV}_4\text{S}_8$ , all the tetrahedra are elongated along the same three-fold rotation axis and the crystal structure changes to polar  $R3m$  in the low-temperature phase, where two different V sites form larger and smaller  $\text{VS}_6$  octahedra with a ratio of 1:3 (Figure S4 in Supporting Information).<sup>11</sup> If the V site with the larger (smaller) volume of the octahedron is assigned to the  $\text{V}^{3+}$  ( $\text{V}^{4+}$ ) ion with two (one) 3d electrons, considering the ionic radius,<sup>33</sup> the total number of 3d electrons per  $\text{V}_4$  cluster becomes  $5e$ , which differs from the intermediate-temperature phase of  $\text{GaNb}_4\text{Se}_8$  with  $7e$  per  $\text{Nb}_4$  cluster. Therefore, the low-temperature phase in  $\text{GaV}_4\text{S}_8$  is not explained by the charge ordering picture but by the simple cooperative Jahn-Teller distortion of the  $\text{V}_4$  molecular orbitals.

In the case of  $\text{CsW}_2\text{O}_6$ , each  $\text{W}^{5.33+}$  trimer forms a three-centered-two-electron state and the rest of W ions behave as  $\text{W}^{6+}$  with empty 5d orbitals below the metal-insulator transition temperature, resulting in a non-magnetic insulating state.<sup>9</sup> Therefore, the trimer formation and the non-magnetic state simultaneously emerge. In  $\text{GaNb}_4\text{Se}_8$ , a non-magnetic appears below  $T_M = 31$  K, which is lower than the charge ordering temperature  $T_C = 50$  K. The low-temperature non-magnetic state of  $\text{GaNb}_4\text{Se}_8$  may originate from the rearrangement of

charges. One may note that the undistorted paramagnetic phase may change directly into non-magnetic states in  $\text{GaNb}_4\text{S}_8$ <sup>26</sup> and  $\text{GaTa}_4\text{Se}_8$ <sup>15</sup> due to the absence of the charge order phase.

## Conclusions

The crystal structure in the intermediate-temperature phase of  $\text{GaNb}_4\text{Se}_8$  is investigated by synchrotron XRD using a high-quality single crystal. The Nb cluster rearrangement from tetramer to trimer-monomer is driven by the chiral charge order. The  $\text{Nb}^{3+}$  trimer is stabilized by  $\sigma$ -bonding six  $4d$  electrons, while a localized  $S = 1/2$  spin remains on the  $\text{Nb}^{4+}$  ion. The chiral charge order maintains the cubic symmetry, which is not found in other lacunar spinel  $\text{GaM}_4\text{X}_8$  series.

Corresponding Author

\*kitou@edu.k.u-tokyo.ac.jp

Notes

The authors declare no competing financial interest.

## ACKNOWLEDGMENT

We thank H. Ishikawa and Y. Okamoto for fruitful discussions, and A. Ikeda for generously allowing us to use an optical sensing instrument (Hyperion si155, LUNA) for thermal expansion. This work was supported by Grants-in-Aid for Scientific Research (No. JP19H05826, JP22K14010, and JP23K13068) from JSPS. The synchrotron radiation experiments were performed at SPring-8 with the approval of the Japan Synchrotron Radiation Research Institute (JASRI) (Proposal No. 2023B1603).



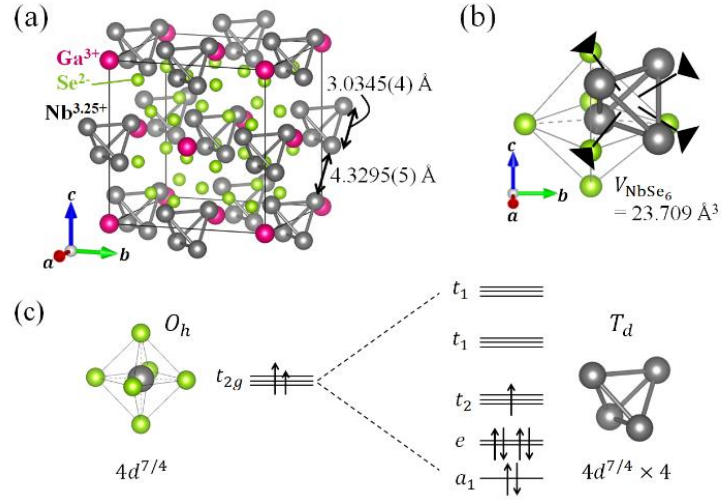


**Figure 1.** (a) Crystal structure of GaNb<sub>4</sub>Se<sub>8</sub> at 70 K in the high-temperature phase. (b) Nb<sub>4</sub> tetrahedron (gray) and Se<sub>6</sub> octahedron (green) in GaNb<sub>4</sub>Se<sub>8</sub>. Solid triangles indicate three-fold rotation axes along  $\langle 111 \rangle$ . (c) Schematic of the molecular orbital formation of the Nb tetramer. The  $t_{2g}$  atomic orbitals under  $O_h$  symmetry at four Nb sites form five molecular orbitals with different energies under  $T_d$  symmetry.

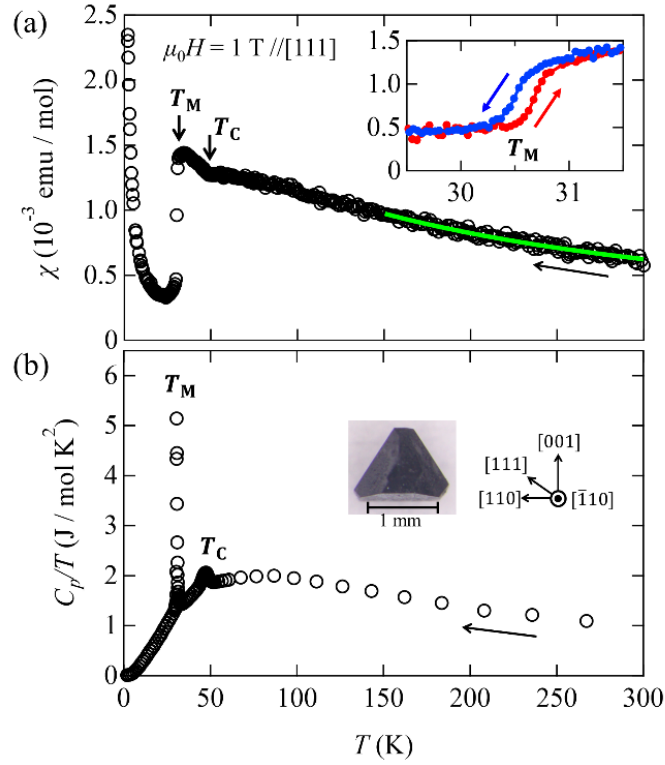


**Figure 2.** (a) Temperature dependence of the magnetic susceptibility  $\chi$  for  $H \parallel [111]$  of  $\text{GaNb}_4\text{Se}_8$ . A yellow-green line indicates the Curie-Weiss fit above 150 K. The inset shows an enlarged view of the behavior around  $T_M$ . Blue and red circles indicate the data in cooling and heating processes, respectively. (b) Temperature dependence of the heat capacity divided by temperature,  $C_p/T$ , at 0 T. The inset shows a single crystal used for the magnetic susceptibility and heat capacity measurements

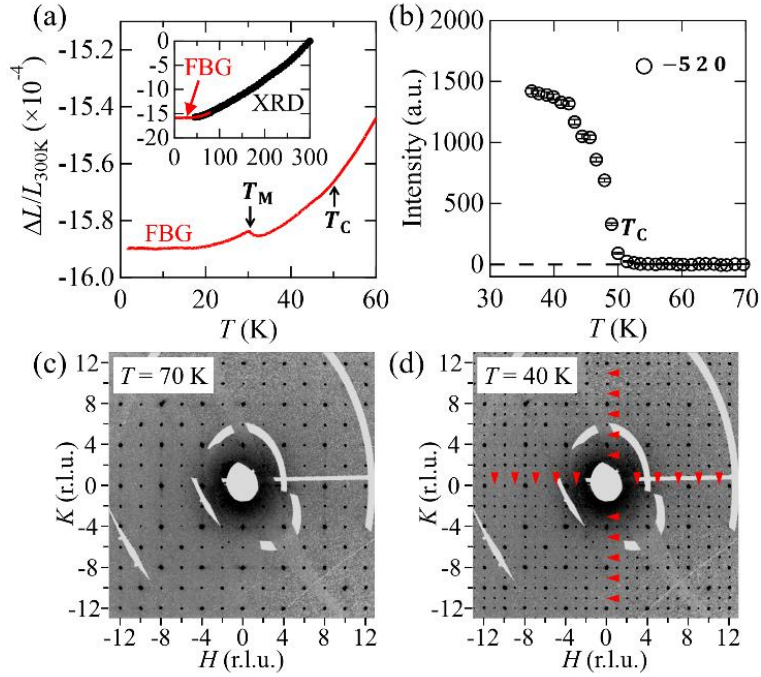


**Figure 3.** (a) Temperature dependence of thermal expansion  $\Delta L/L_{300\text{K}}$  along the [111] axis of  $\text{GaNb}_4\text{Se}_8$ . The inset shows the data up to 300 K. Black dots and red lines indicate the XRD and FBG data, respectively. (b) Temperature dependence of the integrated intensity of  $-5\ 2\ 0$  reflection. (c,d) XRD data on the  $H\ K\ 0$  plane at (c) 70 K in the high-temperature phase and (d) 40 K in the intermediate-temperature phase. Red triangles in (d) indicate positions  $h00: h = 2n + 1$  and  $0k0: k = 2n + 1$ , where no Bragg peaks are observed.

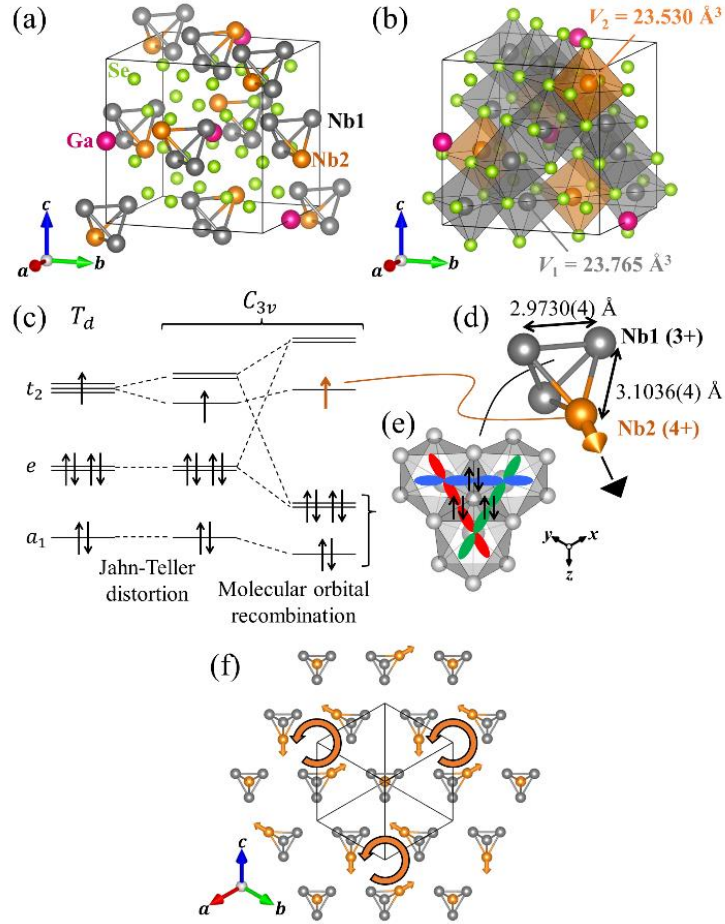


**Figure 4.** Crystal structure of  $\text{GaNb}_4\text{Se}_8$  at 40 K in the intermediate-temperature phase, focusing on (a)  $\text{Nb}_4$  tetrahedra and (b)  $\text{NbSe}_6$  octahedra. (c) Schematic of the molecular orbital recombination indicating the Nb cluster rearrangement from a tetramer to a trimer-monomer. (d) A distorted  $\text{Nb}_4$  tetrahedron around  $1/2, 0, 1/2$  composed of a Nb1 trimer (gray) and a Nb2 atom (orange). A solid triangle indicates the three-fold rotation axis, along which a local electric dipole moment is present (an orange vector). (e) Schematic of a spin-singlet formation in a Nb1 trimer. Red, green, and blue ribbons indicate the  $d_{yz}$ ,  $d_{zx}$ , and  $d_{xy}$  orbitals extending in the trimer plane, respectively. The  $x$ ,  $y$ , and  $z$  vectors indicate the local axes. (f) Vortex arrangement of electric dipole moments at tetramers on a (111) layer.

## REFERENCES

1. Streltsov, S. V.; Khomskii, D. I. Orbital physics in transition metal compounds: new trends. *Phys.-Usp.* **2017**, 60, 1121.
2. Khomskii, D. I.; Streltsov, S. V. Orbital Effects in Solids: Basics, Recent Progress, and Opportunities. *Chem. Rev.* **2021**, 121, 2992-3030.
3. Andersson G. Studies on Vanadium Oxides. *Acta Chim. Scand.* **1956**, 10, 623.
4. Kawakubo, T. Crystal Distortion and Electric and Magnetic Transition in VO<sub>2</sub>. *J. Phys. Soc. Jpn.* **1965**, 20, 516.
5. Longo, J. M.; Kierkegaard, P. A Refinement of Structure of VO<sub>2</sub>. *Acta Chem. Scand.* **1970**, 24, 420.
6. Kucharczyk, D.; Niklewski, T. Accurate X-ray Determination of the Lattice Parameters and the Thermal Expansion Coefficients of VO<sub>2</sub> near the Transition Temperature. *J. Appl. Cryst.* **1979**, 12, 370.
7. Kitou, S; Nakano, A; Imaizumi, M.; Nakamura, Y.; Terasaki, I.; Arima, T. Molecular orbital formation and metastable short-range ordered structure in VO<sub>2</sub>. *arXiv:2310.10193*.
8. Hirai, D.; Bremholm, M.; Allred, J. M.; Krizan, J.; Schoop, L. M.; Huang, Q.; Tao, J.; Cava, R. J. Spontaneous Formation of Zigzag Chains at the Metal-Insulator Transition in the  $\beta$ -Pyrochlore CsW<sub>2</sub>O<sub>6</sub>. *Phys. Rev. Lett.* **2013**, 110, 166402.
9. Okamoto, Y.; Amano, H.; Katayama, N.; Sawa, H.; Niki, K.; Mitoka, R.; Harima, H.; Hasegawa, T.; Ogita, N.; Tanaka, Y.; Takigawa, M.; Yokoyama, Y.; Takehana, K.; Imanaka, Y.; Nakamura, Y.; Kishida, H.; Takenaka, K. Electrical and Thermal Transport Properties of the  $\beta$ -Pyrochlore Oxide CsW<sub>2</sub>O<sub>6</sub>. *Nat. Commun.* **2020**, 11, 3144.
10. Abd-Elmeguid, M. M.; Ni, B.; Khomskii, D. I.; Pocha, R.; Johrendt, D.; Wang, X.; Syassen, K. Transition from Mott Insulator to Superconductor in GaNb<sub>4</sub>Se<sub>8</sub> and GaTa<sub>4</sub>Se<sub>8</sub> under High Pressure. *Phys. Rev. Lett.* **2004**, 93, 126403.
11. Pocha, R.; Johrendt, D.; Ni, B.; Abd-Elmeguid, M. M. Crystal Structures, Electronic Properties, and Pressure-Induced Superconductivity of the Tetrahedral Cluster Compounds GaNb<sub>4</sub>S<sub>8</sub>, GaNb<sub>4</sub>Se<sub>8</sub>, and GaTa<sub>4</sub>Se<sub>8</sub>. *J. Am. Chem. Soc.* **2005**, 127, 8732-8740.

12. Park, M. J.; Sim, G.; Jeong, M. Y.; Mishra, A.; Han, M. J.; Lee, S. Pressure-induced topological superconductivity in the spin-orbit Mott insulator GaTa<sub>4</sub>Se<sub>8</sub>. *npj Quantum Mater.* **2020**, 5, 41.
13. Deng, H.; Zhang, J.; Jeong, M. Y.; Wang, D.; Hu, Q.; Zhang, S.; Sereika, R.; Nakagawa, T.; Chen, B.; Yin, X.; Xiao, H.; Hong, X.; Ren, J.; Han, M. J.; Chang, J.; Weng, H.; Ding, Y.; Lin, H.-Q.; Mao, H.-k. Metallization of Quantum Material GaTa<sub>4</sub>Se<sub>8</sub> at High Pressure. *J. Phys. Chem. Lett.* **2021**, 12, 5601-5607.
14. Waki, T.; Kajinami, Y.; Tabata, Y.; Nakamura, H.; Yoshida, M.; Takigawa, M.; Watanabe, I. Spin-singlet state formation in the cluster Mott insulator GaNb<sub>4</sub>S<sub>8</sub> studied by  $\mu$ SR and NMR spectroscopy. *Phys. Rev. B* **2010**, 81, 020401(R).
15. Ishikawa, H.; Yajima, T.; Matsuo, A.; Ihara, Y.; Kindo, K. Nonmagnetic Ground States and a Possible Quadrupolar Phase in 4d and 5d Lacunar Spinel Selenides GaM<sub>4</sub>Se<sub>8</sub> (M = Nb, Ta). *Phys. Rev. Lett.* **2020**, 124, 227202.
16. Kim, H.-S.; Im, J.; Han, M. J.; Jin, H. Spin-orbital entangled molecular  $j_{\text{eff}}$  states in lacunar spinel compounds. *Nat. Commun.* **2014**, 5, 3988.
17. Jeong, M. Y.; Chang, S. H.; Kim, B. H.; Sim, J.-H.; Said, A.; Casa, D.; Gog, T.; Janod, E.; Cario, L.; Yunoki, S.; Han, M. J.; Kim, J. Direct experimental observation of the molecular  $J_{\text{eff}} = 3/2$  ground state in the lacunar spinel GaTa<sub>4</sub>Se<sub>8</sub>. *Nat. Commun.* **2017**, 8, 782.
18. Petersen, T.; Prodan, L.; Tsurkan, V.; Krug von Nidda, H.-A.; Kézsmárki, I.; Röbber, U. K.; Hozoi, L. How Correlations and Spin-Orbit Coupling Work within Extended Orbitals of Transition-Metal Tetrahedra of 4d/5d Lacunar Spinels. *J. Phys. Chem. Lett.* **2022**, 13, 1681-1686.
19. Petersen, T.; Bhattacharyya, P.; Röbber, U. K.; Hozoi, L. Resonating holes vs molecular spin-orbit coupled states in group-5 lacunar spinels. *Nat. Commun.* **2023**, 14, 5218.
20. Yang, T.-H.; Kawamoto, S.; Higo, T.; Wang, S. G.; Stone, M. B.; Neuefeind, J.; Ruff, J. P. C.; Abeykoon, A. M. M.; Chen, Y.-S.; Nakatsuji, S.; Plumb, K. W. Bond ordering and molecular spin-orbital fluctuations in the cluster Mott insulator GaTa<sub>4</sub>Se<sub>8</sub>. *Phys. Rev. Research* **2022**, 4, 033123.

21. Kézsmárki, I.; Bordács, S.; Milde, P.; Neuber, E.; Eng, L. M.; White, J. S.; Rønnow, H. M.; Dewhurst, C. D.; Mochizuki, M.; Yanai, K.; Nakamura, H.; Ehlers, D.; Tsurkan, V.; Loidl, A. Néel-type skyrmion lattice with confined orientation in the polar magnetic semiconductor GaV<sub>4</sub>S<sub>8</sub>. *Nat. Mater.* **2015**, *14*, 1116-1122.
22. Ruff, E.; Widmann, S.; Lunkenheimer, P.; Tsurkan, V.; Bordács, S.; Kézsmárki, I.; Loidl, A. Multiferroicity and skyrmions carrying electric polarization in GaV<sub>4</sub>S<sub>8</sub>. *Sci. Adv.* **2015**, *1*, e1500916.
23. Fujima, Y.; Abe, N.; Tokunaga, Y.; Arima, T. Thermodynamically stable skyrmion lattice at low temperatures in a bulk crystal of lacunar spinel GaV<sub>4</sub>Se<sub>8</sub>. *Phys. Rev. B* **2017**, *95*, 180410(R).
24. Schueller, E. C.; Kitchaev, D. A.; Zuo, J. L.; Bocarsly, J. D.; Cooley, J. A.; Van der Ven, A.; Wilson, S. D.; Seshadri, R. Structural evolution and skyrmionic phase diagram of the lacunar spinel GaMo<sub>4</sub>Se<sub>8</sub>. *Phys. Rev. Materials* **2020**, *4*, 064402.
25. Pocha, R.; Johrendt, D.; Pöttgen, R. Electronic and Structural Instabilities in GaV<sub>4</sub>S<sub>8</sub> and GaMo<sub>4</sub>S<sub>8</sub>. *Chem. Mater.* **2000**, *12*, 2882-2887.
26. Geirhos, K.; Langmann, J.; Prodan, L.; Tsirlin, A. A.; Missiul, A.; Eickerling, G.; Jesche, A.; Tsurkan, V.; Lunkenheimer, P.; Scherer, W.; Kézsmárki, I. Cooperative Cluster Jahn-Teller Effect as a Possible Route to Antiferroelectricity. *Phys. Rev. Lett.* **2021**, *126*, 187601.
27. Sugimoto, K.; Ohsumi, H.; Aoyagi, S.; Nishibori, E.; Moriyoshi, C.; Kuroiwa, Y.; Sawa, H.; Takata, M. Extremely High Resolution Single Crystal Diffractometry for Orbital Resolution using High Energy Synchrotron Radiation at SPring-8. *AIP Conf. Proc.* **2010**, *1234*, 887-890.
28. CrysAlisPro (Agilent Technologies Ltd, Yarnton, 2014).
29. Petříček, V.; Dušek, M.; Palatinus, L. Discontinuous modulation functions and their application for analysis of modulated structures with the computing system JANA2006. *Z. Kristallogr. Cryst. Mater.* **2014**, *229*, 345-352.
30. Momma, K.; Izumi, F. VESTA 3 for three-dimensional visualization of crystal, volumetric and morphology data. *J. Appl. Crystallogr.* **2011**, *44*, 1272-1276.

31. Kim, H.-S.; Haule, K.; Vanderbilt, D. Molecular Mott state in the deficient spinel  $\text{GaV}_4\text{S}_8$ . *Phys. Rev. B* **2020**, 102, 081105(R).
32. Winkler, M.; Prodan, L.; Tsurkan, V.; Lunkenheimer, P.; Kézsmárki, I. Antipolar transitions in  $\text{GaNb}_4\text{Se}_8$  and  $\text{GaTa}_4\text{Se}_8$ . *Phys. Rev. B* **2022**, 106, 115146.
33. Shannon, R. D. Revised effective ionic radii and systematic studies of interatomic distances in halides and chalcogenides. *Acta Crystallogr.* **1976**, 32, 751-767.
34. Pen, H. F.; van den Brink, J.; Khomskii, D. I.; Sawatzky, G. A. Orbital Ordering in a Two-Dimensional Triangular Lattice. *Phys. Rev. Lett.* **1997**, 78, 1323.
35. Goodenough, J. B.; Dutta, G.; Manthiram, A. Lattice instabilities near the critical V-V separation for localized versus itinerant electrons in  $\text{LiV}_{1-y}\text{M}_y\text{O}_2$  ( $\text{M} = \text{Cr}$  or  $\text{Ti}$ )  $\text{Li}_{1-x}\text{VO}_2$ . *Phys. Rev. B* **1991**, 43, 10170.
36. Katayama, N.; Uchida, M.; Hashizume, D.; Niitaka, S.; Matsuno, J.; Matsumura, D.; Nishihata, Y.; Mizuki, J.; Takeshita, N.; Gauzzi, A.; Nohara, M.; Takagi, H. Anomalous Metallic State in the Vicinity of Metal to Valence-Bond Solid Insulator Transition in  $\text{LiVS}_2$ . *Phys. Rev. Lett.* **2009**, 103, 146405.



# Supporting Information of

## Cluster rearrangement by chiral charge order in lacunar spinel GaNb<sub>4</sub>Se<sub>8</sub>

Shunsuke Kitou<sup>1</sup>, Masaki Gen<sup>2</sup>, Yuiga Nakamura<sup>3</sup>, Yusuke Tokunaga<sup>1</sup>, Taka-hisa Arima<sup>1,2</sup>

<sup>1</sup>*Department of Advanced Materials Science, The University of Tokyo, Kashiwa 277-8561, Japan.*

<sup>2</sup>*RIKEN Center for Emergent Matter Science, Wako 351-0198, Japan.*

<sup>3</sup>*Japan Synchrotron Radiation Research Institute (JASRI), SPring-8; Hyogo 679-5198, Japan.*

Table S1. Structural parameters of GaNb<sub>4</sub>Se<sub>8</sub> at 70 K. The space group is  $F\bar{4}3m$  (No. 216) and  $a = 10.4143(11)$  Å. Note that  $U_{11} = U_{22} = U_{33}$  and  $U_{12} = U_{13} = U_{23}$ .

Atom	Wyckoff position	Site symmetry	$x$	$y$	$z$	$U_{11}$ (Å <sup>2</sup> )	$U_{12}$ (Å <sup>2</sup> )
Ga	4a	$\bar{4}3m$	0	0	0	0.003035(13)	0
Nb	16e	.3m	0.396982(4)	= $x$	= $x$	0.004115(8)	-0.000372(6)
Se1	16e	.3m	0.635612(5)	= $x$	= $x$	0.004135(9)	0.000178(8)
Se2	16e	.3m	0.134355(4)	= $x$	= $x$	0.003183(8)	-0.000248(7)

Table S2. Summary of crystallographic data of GaNb<sub>4</sub>Se<sub>8</sub> at 70 K.

Wavelength (Å)	0.30956 Å
Crystal dimension (μm <sup>3</sup> )	52×48×35
Space group	$F\bar{4}3m$
$a$ (Å)	10.4143(11)
$Z$	4
$F(000)$	1868
$(\sin\theta/\lambda)_{\max}$ (Å <sup>-1</sup> )	1.79
$N_{\text{total}}$	44710
$N_{\text{unique}}$	2629
Average redundancy	17.006
Completeness (%)	100
Number of unique reflections ( $I > 3\sigma$ / all)	2575 / 2629
Assuming Ga occupancy = 1 ( $N_{\text{parameters}} = 12$ )	
$R_1$ ( $I > 3\sigma$ / all)	2.14% / 2.17%
$wR_2$ ( $I > 3\sigma$ / all)	2.46% / 2.47%
GOF ( $I > 3\sigma$ / all)	1.76 / 1.74
Flack parameters ( $a, b, c: -a, -b, -c$ ( $\bar{1}$ ))	0.994(12) : 0.006(12)
Allowing Ga deficiency ( $N_{\text{parameters}} = 13$ )	
Occupancy of Ga	0.994(3)
$R_1$ ( $I > 3\sigma$ / all)	2.14% / 2.17%
$wR_2$ ( $I > 3\sigma$ / all)	2.46% / 2.47%
GOF ( $I > 3\sigma$ / all)	1.75 / 1.74

Table S3. Structural parameters of GaNb<sub>4</sub>Se<sub>8</sub> at 40 K. The space group is  $P2_13$  (No. 198) and  $a = 10.4138(11)$  Å.

Atom	Wyckoff position	Site symmetry	$x$	$y$	$z$
Ga	4a	.3.	0.498942(6)	= $x$	= $x$
Nb1	12b	1	0.598205(4)	0.895622(3)	0.602942(4)
Nb2	4a	.3.	0.893013(5)	= $x$	= $x$
Se1	12b	1	0.635199(5)	0.368042(5)	0.362978(5)
Se2	12b	1	0.634497(5)	0.868026(5)	0.363490(5)
Se3	4a	.3.	0.633245(5)	= $x$	= $x$
Se4	4a	.3.	0.139546(6)	= $x$	= $x$

Atom	$U_{11}$ (Å <sup>2</sup> )	$U_{22}$ (Å <sup>2</sup> )	$U_{33}$ (Å <sup>2</sup> )	$U_{12}$ (Å <sup>2</sup> )	$U_{13}$ (Å <sup>2</sup> )	$U_{23}$ (Å <sup>2</sup> )
Ga	0.002251(8)	= $U_{11}$	= $U_{11}$	-0.000016(8)	= $U_{12}$	= $U_{12}$
Nb1	0.002112(9)	0.002401(10)	0.002292(11)	0.000014(6)	-0.000032(8)	-0.000403(9)
Nb2	0.002686(8)	= $U_{11}$	= $U_{11}$	-0.000148(7)	= $U_{12}$	= $U_{12}$
Se1	0.002149(12)	0.002187(10)	0.002192(13)	0.000077(8)	0.000145(8)	-0.000133(9)
Se2	0.002640(14)	0.002726(12)	0.002549(12)	-0.000074(10)	0.000325(9)	0.000021(9)
Se3	0.002193(9)	= $U_{11}$	= $U_{11}$	-0.000123(9)	= $U_{12}$	= $U_{12}$
Se4	0.002430(9)	= $U_{11}$	= $U_{11}$	0.000004(9)	= $U_{12}$	= $U_{12}$

Table S4. Summary of crystallographic data of GaNb<sub>4</sub>Se<sub>8</sub> at 40 K.

Wavelength (Å)	0.30956 Å
Crystal dimension (μm <sup>3</sup> )	52×48×35
Space group	<i>P</i> 2 <sub>1</sub> 3
<i>a</i> (Å)	10.4138(11)
<i>Z</i>	4
<i>F</i> (000)	1868
(sinθ/λ) <sub>max</sub> (Å <sup>-1</sup> )	1.79
<i>N</i> <sub>total</sub>	178930
<i>N</i> <sub>unique</sub>	17764
Average redundancy	17.006
Completeness (%)	99.56
<i>N</i> <sub>parameters</sub>	43
Number of unique reflections ( <i>I</i> >3σ / all)	17159 / 17764
<i>R</i> <sub>1</sub> ( <i>I</i> >3σ / all)	2.24% / 2.34%
<i>wR</i> <sub>2</sub> ( <i>I</i> >3σ / all)	2.67% / 2.69%
GOF ( <i>I</i> >3σ / all)	1.23 / 1.22
Flack parameters	0.490(15) : 0.008(8)
( <i>a, b, c</i> : - <i>a, -b, -c</i> ( $\bar{1}$ ): - <i>b, -a, c</i> ( <i>.m</i> ): <i>b, a, -c</i> ( <i>.2</i> ))	: 0.499(8) : 0.003(8)

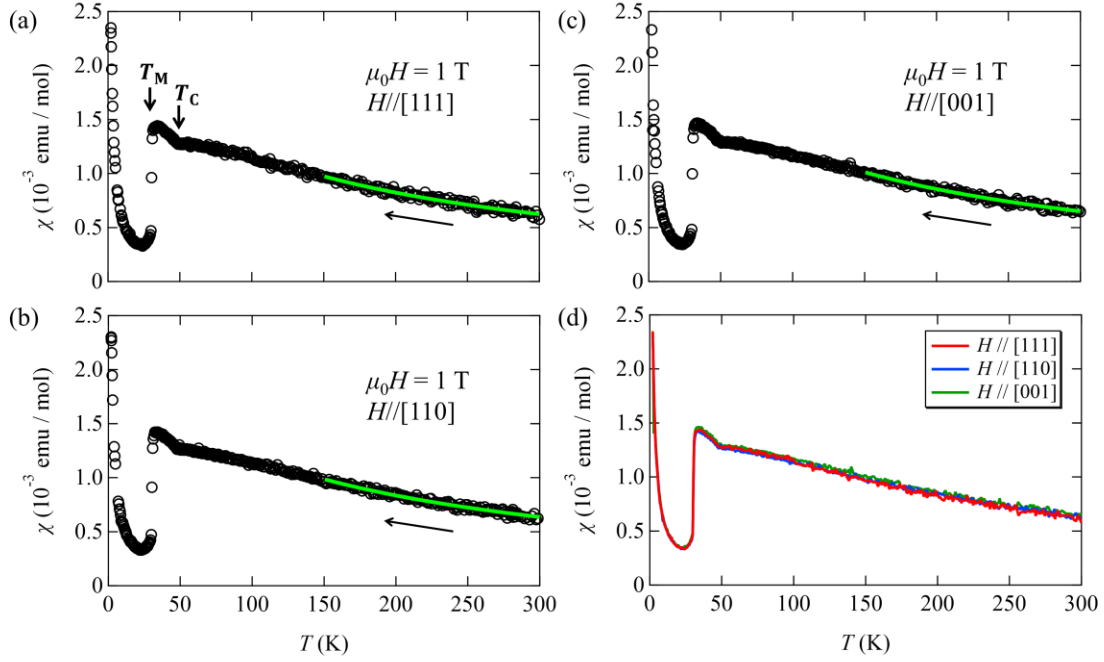


Figure S1. Temperature dependence of the magnetic susceptibility  $\chi$  for (a)  $H \parallel [111]$ , (b)  $H \parallel [110]$ , and (c)  $H \parallel [001]$  of  $\text{GaNb}_4\text{Se}_8$ . Yellow-green lines indicate the results of Curie-Weiss fits above 150 K. (d) The three sets of data (a)-(c) are displayed overlapping.

Table S5. Summary of Curie-Weiss fits for the magnetic susceptibility using a formula  $\chi(T) = \chi_0 + C/(T - \Theta)$ , where  $\chi_0$ ,  $C$ , and  $\Theta$  indicate temperature independent terms of  $\chi$ , Curie constant, and Weiss temperature.

	$\chi_0$ [emu/mol]	$C$ [K emu/mol]	$\Theta$ [K]	$\mu_{\text{eff}}$ [ $\mu_B/\text{f. u.}$ ]
$H \parallel [111]$	$-6.2 \times 10^{-5}$	0.3033	-142.6	1.558
$H \parallel [110]$	$-4.6 \times 10^{-5}$	0.3024	-143.1	1.555
$H \parallel [001]$	$-4.7 \times 10^{-5}$	0.3063	-139.2	1.565

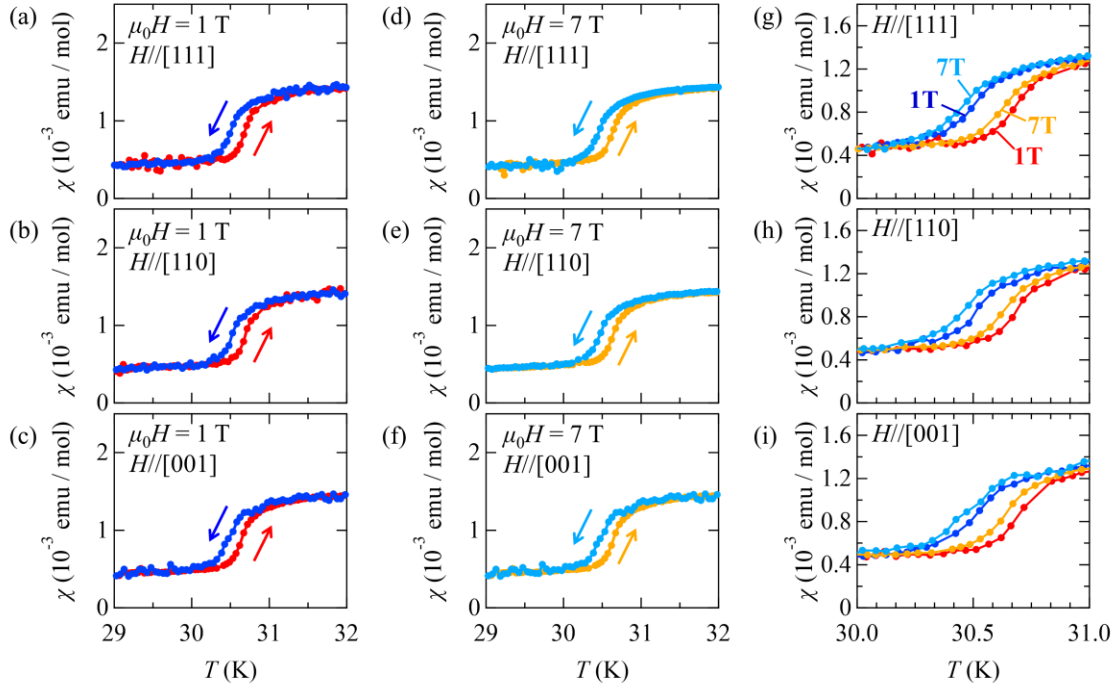


Figure S2. Enlarged views of temperature dependence of the magnetic susceptibility  $\chi$  for (a)  $H \parallel [111]$ , (b)  $H \parallel [110]$ , and (c)  $H \parallel [001]$  under the application of  $\mu_0 H = 1$  T, and for (d)  $H \parallel [111]$ , (e)  $H \parallel [110]$ , and (f)  $H \parallel [001]$  under the application of  $\mu_0 H = 7$  T. (g)-(i) The data for different external magnetic fields are displayed overlapping. The entropy change at  $T_M$  is estimated from the temperature dependence and the external magnetic field dependence of the magnetic susceptibilities using the Clausius-Clapeyron equation  $\Delta S_M = -\Delta M \cdot dB/dT_M$ .  $\Delta M$  is calculated using the average difference in the magnetization before and after the magnetic phase transition at  $\mu_0 H = 1$  T and 7 T. Since  $\Delta M = 0.034$  J/mol T and  $dB/dT_M = 6$  T/ $-0.03$  K are estimated from  $\chi$  for  $H \parallel [111]$  under  $\mu_0 H = 1$  T and 7 T, the magnetic entropy change is calculated as  $\Delta S_M = 6.8$  J/mol K, which is comparable to the total magnetic entropy  $R \ln 2 \cong 5.76$  J/mol K expected for  $S_{\text{eff}} = 1/2$ .

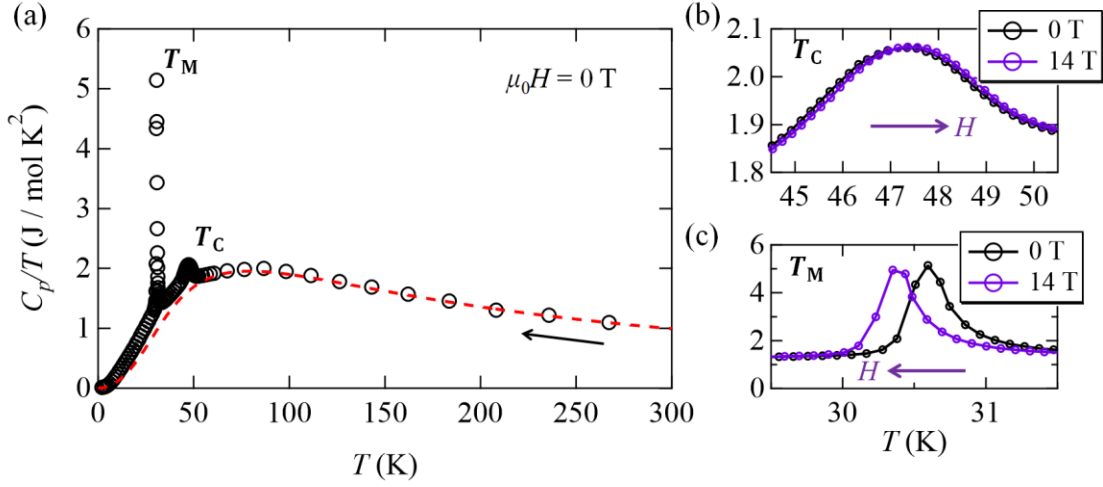


Figure S3. (a) Temperature dependence of the heat capacity divided by temperature  $C_p/T$  at 0 T. The data were obtained in a cooling run. The red dashed line denotes the estimated lattice heat capacity  $C_{\text{fit}}$  based on a two-phonon Debye model. Here, the fitting functions are defined as  $C_{\text{fit}} = \frac{1}{3}C_{D_1} + \frac{2}{3}C_{D_2}$ , and  $C_{D_i} = 9Nk_B \left(\frac{T}{\Theta_{D_i}}\right)^3 \int_0^{\Theta_{D_i}/T} \frac{x^4 e^x}{(e^x - 1)^2} dx$ , where  $N = 13$  is the number of atoms in the formula unit. The obtained fitting parameters are  $\Theta_{D_1} = 600$  K and  $\Theta_{D_2} = 250$  K. As mentioned in the main manuscript, the Debye model fails to reproduce the experimental data because a  $T$ -bilinear component appears at low temperatures. (b,c) Enlarged views around (b)  $T_C$  and (c)  $T_M$ . Black and purple dots indicate  $C_p/T$  for  $H = 0$  and for  $\mu_0 H = 14$  T along [111], respectively.  $T_M$  decreases with increasing the external magnetic fields, while  $T_C$  slightly increases.

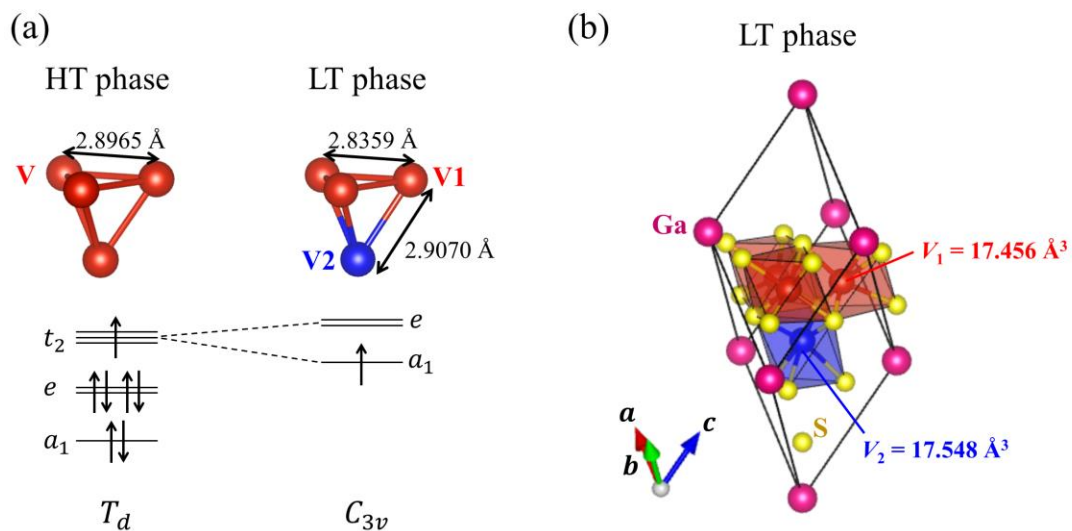


Figure S4. Schematic of a cooperative Jahn-Teller distortion of the  $t_2$  molecular orbitals and crystal structure of  $\text{GaV}_4\text{S}_8$  at 20 K in the low-temperature phase, referred from [1]. The volumes of  $\text{V1S}_6$  and  $\text{V2S}_6$  octahedra are 17.456 and 17.548  $\text{\AA}^3$ , respectively, which contradicts the model of  $\text{V}^{3+}$  trimer- $\text{V}^{4+}$  monomer formation.

## References

1. Pocha, R.; Johrendt, D.; Pöttgen, R. Electronic and Structural Instabilities in  $\text{GaV}_4\text{S}_8$  and  $\text{GaMo}_4\text{S}_8$ . *Chem. Mater.* **2000**, 12, 2882.